ACS Chemical Neuroscience

pubs.acs.org/chemneuro Research Article

Curcumin Reduces Amyloid Beta Oligomer Interactions with Anionic Membranes

Chad A. Sallaberry, Barbie J. Voss, William B. Stone, Fabiola Estrada, Advita Bhatia, J. Daniel Soto, Charles W. Griffin, and Crystal M. Vander Zanden*

Cite This: *ACS Chem. Neurosci.* 2023, 14, 4026–4038 Read Online

ACCESS | Metrics & More | Article Recommendations | Supporting Information

ABSTRACT: Many neurodegenerative diseases involve amyloidogenic proteins forming surface-bound aggregates on anionic membranes, and the peptide amyloid β (Aβ) in Alzheimer's disease is one prominent example of this. Curcumin is a small polyphenolic molecule that provides an interesting opportunity to understand the fundamental mechanisms of membrane-mediated aggregation because it embeds into membranes to alter their structure while also altering Aβ aggregation in an aqueous environment. The purpose of this work was to understand interactions among curcumin, β-sheet-rich Aβ fibrillar oligomers (FO), and a model anionic membrane. From a combination of liquid surface X-ray scattering experiments and molecular dynamics simulations, we found that curcumin embedded into an anionic 1,2-dimyristoyl-*sn*-glycero-3-phosphorylglycerol (DMPG) membrane to rest between the lipid headgroups and the tails, causing disorder and membrane thinning. FO accumulation on the membrane was reduced by ~66% in the presence of curcumin, likely influenced by membrane thinning. Simulation results suggested curcumin clusters near exposed phenylalanine residues on a membrane-embedded FO structure. Altogether, curcumin inhibited FO interactions with a DMPG membrane, likely through a combination of altered membrane structure and interactions with the FO surface. This work elucidates the mechanism of curcumin as a small molecule that inhibits amyloidogenesis through a combination of both membrane and protein interactions.

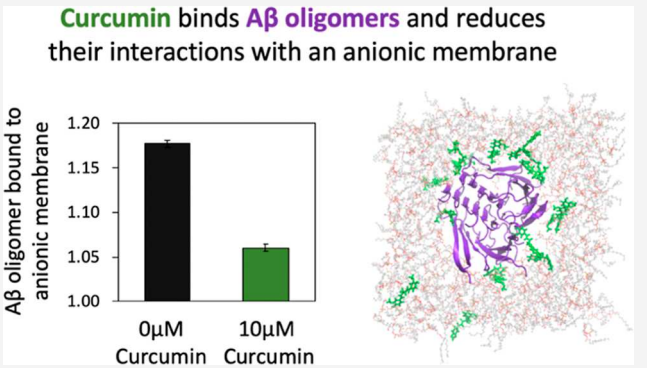

KEYWORDS: *amyloid beta, lipid membranes, curcumin, X-ray reflectivity, grazing incidence X-ray diffraction, molecular dynamics*

INTRODUCTION

Alzheimer's disease (AD) is the most prevalent in a family of neurodegenerative diseases that share a common theme of neurotoxic protein misfolding into an amyloidogenic form. The amyloid cascade hypothesis is the most supported mechanism to explain the neurodegeneration observed in AD, with decades of research investigating the idea that the proteins amyloid beta (Aβ) and tau misfold into β-sheet-rich amyloid structures.[1,2] Many other important factors also contribute to AD, likely including microglia-mediated neuroinflammation, Apoε4 allele prevalence, exposure to heavy metal toxins, the gut−brain axis, and many more. However, the theme of protein misfolding into amyloid structures is inescapable considering that amyloidogenic misfolding is also observed for the protein α-synuclein in Parkinson's disease, prion protein in prion diseases, huntingtin protein in Huntington's chorea, and SOD1 and other proteins in amyotrophic lateral sclerosis.[3,4]

The amyloid cascade hypothesis posits that a monomeric protein misfolds into β-sheet-rich oligomers, and those oligomers grow into larger amyloid fibrils.[1,2] In AD, the oligomers are generally accepted as the most toxic species to cell and animal models;[5−8] therefore, there is substantial interest in reducing the toxicity of these oligomers and preventing their formation. In this study, Aβ 1−40 was selected for its slower aggregation kinetics, which allows us to accurately assess the monomeric (Aβ_m) and β-sheet-rich oligomer states.[9]

Aβ and tau interact with cell membranes to nucleate the formation of β-sheet-rich structures,[10−15] and in vitro studies report that membranes accelerate fibrillation.[10,14,16] Aβ_m interacts with anionic membranes, such as PS, PG, or ganglioside lipids, through a combination of favorable interactions with the hydrophobic lipid tails and the charged lipid headgroups.[14,17−19] Oligomers also bind to anionic membranes and cause more disruption to membrane structure compared to monomers.[11] Consequently, Aβ interactions

Received: August 3, 2023
Revised: October 7, 2023
Accepted: October 12, 2023
Published: October 31, 2023

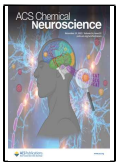

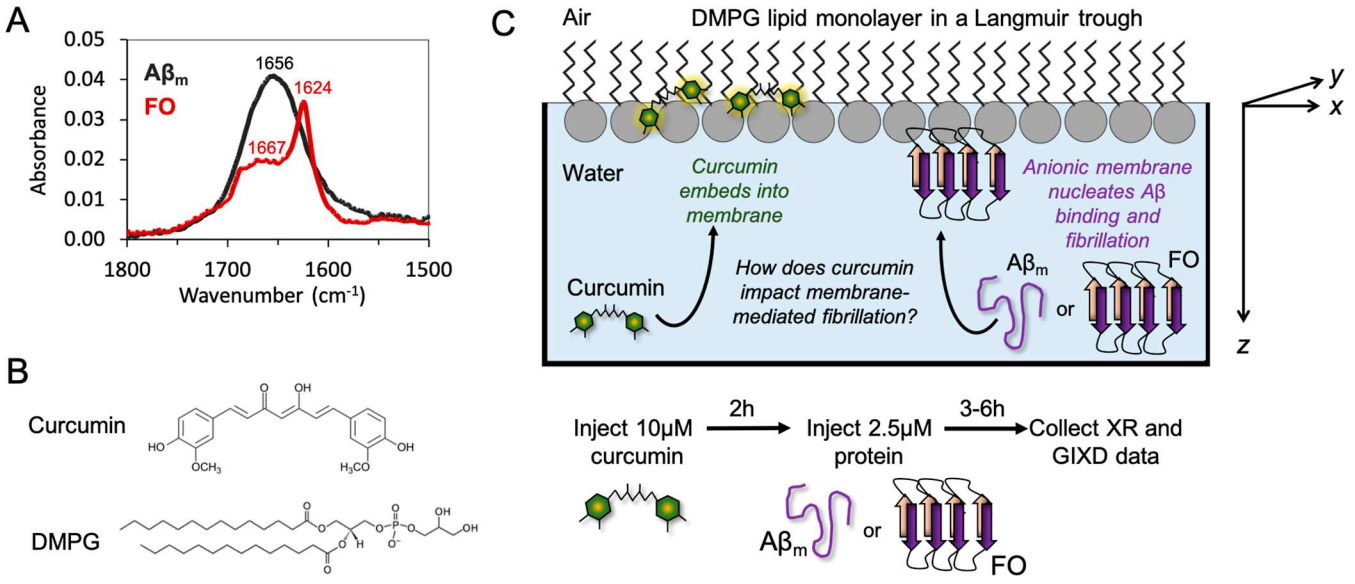

Figure 1. Confirmation of monomeric amyloid beta ($A\beta_m$) and FO structures and an overview of the experimental design. (A) FTIR data for $A\beta_m$ solubilized in DMSO and preformed FOs in water. The FO peak at 1624 cm^{-1} is distinctly characteristic of β-sheets. (B) Chemical structures of curcumin and 1,2-dimyristoyl-*sn*-glycero-3-phosphorylglycerol (DMPG). (C) Schematic of the experimental design. A DMPG lipid monolayer was deposited at the air/water interface in a Langmuir trough to a surface pressure of 25 mN/m. 10 μM curcumin was injected into the water subphase and incubated for 2 h. $A\beta_m$ or FO (2.5 mM) was then injected into the subphase and allowed to bind the membrane, comparing interactions with a pure membrane or a membrane containing curcumin.

change the membrane structure, resulting in a variety of impacts on the cell, from altering cell signaling[20−22] to membrane thinning and pore formation.[6,11,16,23−25] Membrane binding and amyloid nucleation are well documented for Aβ; however, this is also observed for tau, α-synuclein, and other amyloidogenic proteins involved in neurodegenerative disease.[12,13,15,26−29]

The polyphenolic molecule curcumin has gained popular attention as a medicinal compound found in turmeric, which has been used in Eastern Medicine for the last 4000 years.[30] Regardless of the clinical efficacy of curcumin for AD treatment, we see this as a unique opportunity to better understand the fundamental mechanism of interactions of amyloidogenic proteins with membranes and how they can be inhibited by small molecules. There are a few noncompeting hypotheses about how curcumin reduces Aβ neurotoxicity for in vitro and in vivo AD models. It is well established that curcumin directly interacts with monomeric, oligomeric, and fibrillar forms of Aβ.[31] However, reports vary in their findings, reporting curcumin preventing aggregation, restructuring Aβ aggregates, and disassembling aggregates. Curcumin also embeds into membranes, causing thinning and increased membrane fluidity. Curcumin binds approximately parallel to the membrane and perpendicular to the lipid tails, positioning itself just beneath the glycerol moiety. Importantly, curcumin alters the behavior of bound proteins due to its impacts on membrane strucutres.[32] A complete discussion and additional references describing curcumin interactions with membranes and Aβ are provided in the Supporting Information.

Given that curcumin independently binds both soluble Aβ and membranes, it is necessary to investigate its interactions with Aβ in a membrane system. This has been studied using Aβ 25−35, which is thought to be the predominant segment required for β-sheet formation and toxicity. Curcumin reduced the amount of β-sheet-rich structures formed on the membrane surface, measured by circular dichroism spectroscopy, thioflavin T fluorescence, and X-ray diffraction.[33,34] This reduction in Aβ 25−35 aggregation was attributed to curcumin's thinning effect on the membrane, suggesting monomeric Aβ preferentially inserts into thicker and more ordered membranes.[35] Another study measuring Aβ 1−42 aggregation using thioflavin T and immunoassays showed that curcumin-decorated liposomes reduced Aβ aggregation compared to pure liposomes.[36] Finally, curcumin inhibited Aβ 1−40 interactions with a lipid monolayer, as evidenced by surface pressure measurements.[37]

A remaining question is curcumin's relative effectiveness at inhibiting preformed Aβ oligomers from interacting with an anionic membrane compared to monomers. In this work, we coupled X-ray scattering experiments with molecular dynamics (MD) simulations to investigate the structure of a β-sheet-rich fibrillar oligomer (FO) interacting with curcumin and a lipid membrane. Using X-ray reflectivity (XR) and grazing incidence X-ray diffraction (GIXD), we found that curcumin inhibits binding of both $A\beta_m$ and FO to a model membrane. Simulations predict that curcumin interacts with exposed phenylalanine residues in a membrane-embedded FO structure. Therefore, curcumin is likely reducing FO binding through both impacts on the membrane fluidity and direct binding to the FO surface.

RESULTS AND DISCUSSION

We used a combination of X-ray scattering experiments and MD simulations to study how curcumin impacts the interactions of $A\beta_m$ and FO with anionic membranes. A lipid monolayer deposited at the air/water interface in a Langmuir trough served as the in vitro system for liquid surface XR and GIXD experiments. XR is used to determine the structure of the membrane and any associated proteins through analysis of an electron density profile normal to the membrane. Therefore, this method can be used to measure changes in membrane structure resulting from curcumin interactions and protein

https://doi.org/10.1021/acschemneuro.3c00512
ACS Chem. Neurosci. 2023, 14, 4026−4038

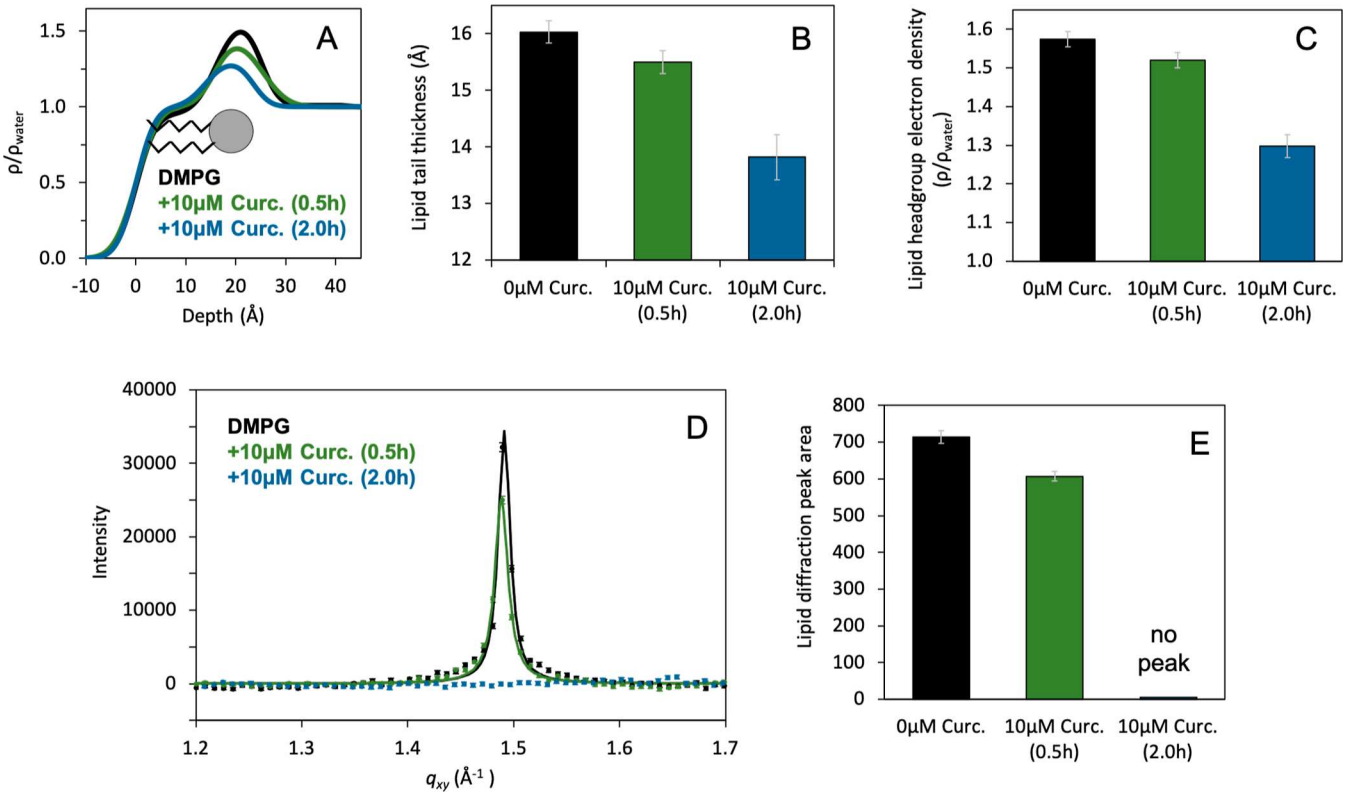

Figure 2. Curcumin binds to a DMPG membrane and reduces lipid ordering. XR and GIXD data were collected from a pure DMPG monolayer deposited at 25 mN/m, and with the addition of 10 μM curcumin after 0.5 and 2 h of incubation. (A) Normalized electron density profiles (ρ/ρ_{water}) that result from reflectivity fitting are plotted as a function of depth along z, normal to the air/water interface. A cartoon lipid is overlaid on the electron density profile. Reflectivity fits are shown in Figure S1A, and XR fit parameters are in Table S2. Lipid tail thickness (B) and headgroup ρ/ρ_{water} (C) parameters from the model-dependent fitting of the XR data. (D) GIXD data are shown as points with experimental error, and the peak fits are overlaid as lines (when applicable). Data are background subtracted. (E) Quantified lipid diffraction peak area. Full GIXD fit parameters and calculated values are reported in Table S5. Error bars in panels (B–E) are the parameter errors obtained from fitting.

accumulation at the membrane surface. GIXD can detect any semicrystalline ordered species present at the membrane, including the repeated 4.7 Å spacing between β-strands in an amyloid β-sheet and lipid tails packed together in a liquid condensed (LC) domain. To complement the in vitro monolayer data, we performed MD simulations of a lipid bilayer interacting with curcumin and FO. Curcumin was pre-embedded into the membrane, and we used the Orientations of Proteins in Membranes (OPM) server to predict a membrane-bound structure for an experimentally determined FO model. With all three components present in our system (lipids, curcumin, and FO), we could determine interactions occurring during 1 μs of simulation.

1,2-Dimyristoyl-*sn*-glycero-3-phosphorylglycerol (DMPG) lipids were used as the model membranes for these studies. At a biologically relevant surface pressure of 25 mN/m,[38] DMPG lipid tails exist in an equilibrium of ordered LC and disordered liquid-expanded (LE) phases. The LC lipids produce a characteristic diffraction peak, meaning that GIXD can be used to determine changes in the amount of lipid packing caused by curcumin or protein interactions. A more biologically relevant membrane containing cholesterol or unsaturated lipids would not have this LC lipid diffraction peak, and a membrane containing saturated lipids with longer tails would contain only the LC phase at biologically relevant surface pressures. Therefore, either of these choices would hinder our ability to use GIXD to detect changes in the membrane structure as a result of curcumin or Aβ binding. Although the lipid monolayer is an obvious limitation of in vitro experiments, it is a suitable model for studying peripheral protein interactions. Aβ forms strong initial interactions with membranes through association with the lipid headgroups and interactions with hydrophobic tails on one leaflet.[39] Therefore, the monolayer is a reasonable choice for investigating early stage Aβ interactions with a membrane containing curcumin.

Intrinsically disordered Aβ_m and preformed β-sheet-rich FOs were made from Aβ 1–40. To confirm the structure of these constructs, Fourier transform infrared spectroscopy (FTIR) was used to probe the amide I absorption band as a readout for protein secondary structure (Figure 1A).[40] Aβ_m had a broad band centered on 1656 cm^{-1}, while the FO displayed a complex amide I profile with a predominate peak at 1624 cm^{-1}, corresponding to random coils and β-sheets, respectively. Altogether, the FO profile observed agrees with previous literature characterizing β-sheet-rich FOs, distinguishing their structures from full-length fibrils or nonfibrillar oligomers.[41−43]

After successful Aβ_m and FO preparations were confirmed, membrane interactions were determined by experiments using X-ray scattering from the air/water interface in a Langmuir trough. In these experiments, a DMPG membrane was deposited on the air/water interface at 25 mN/m, and 10 μM curcumin was injected into the subphase (Figure 1B,C). Previous work has shown that curcumin embeds into lipid membranes, binding beneath the headgroups and increasing lipid tail disorder.[32,44] Aβ_m and FO are also known to interact with anionic membranes, with the anionic membrane

https://doi.org/10.1021/acschemneuro.3c00512
ACS Chem. Neurosci. 2023, 14, 4026−4038

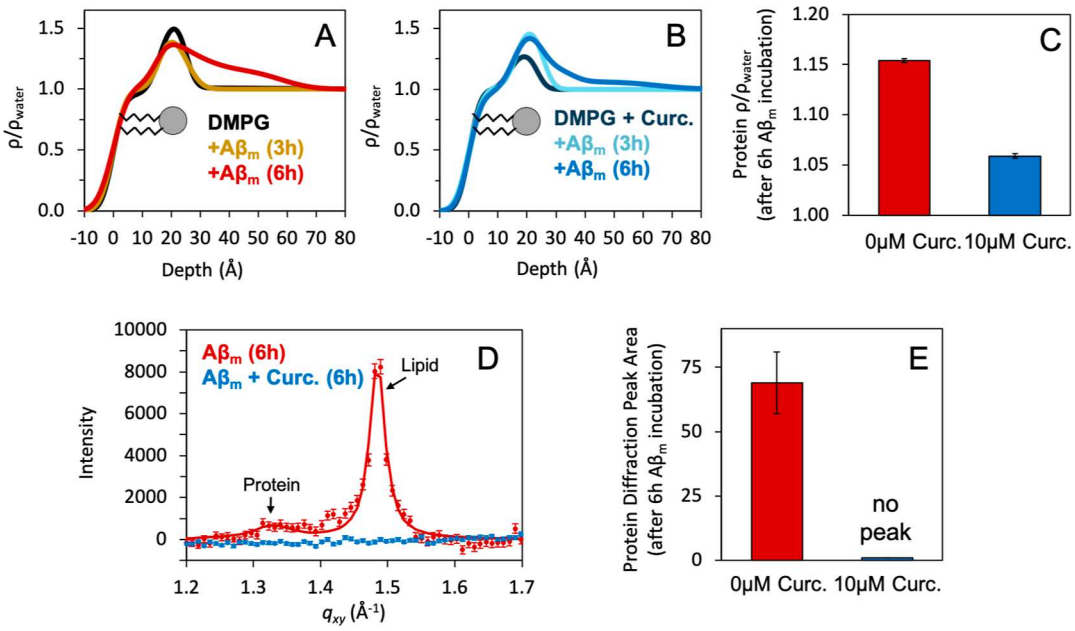

Figure 3. Curcumin reduces A$\beta_m$binding and fibrillation on a DMPG membrane. XR and GIXD data were collected from a pure DMPG monolayer (A) or a monolayer incubated with 10 μM curcumin for 2 h (B). Aβ_m was injected to reach a 2.5 μM subphase concentration, and data was collected after 3 and 6 h of incubation. (A,B) Normalized electron density profiles (ρ/ρ_{water}) are plotted as a function of depth along z, normal to the air/water interface. A cartoon lipid is overlaid onto the electron density profile. Reflectivity fits are shown in Figure S1B,C and XR fit parameters are shown in Table S3. (C) Protein ρ/ρ_{water} parameters were from the model-dependent fitting of the XR data. (D) Background-subtracted GIXD data are shown as points with experimental error, and the peak fits are overlaid as lines (when applicable). Amyloids produce a characteristic diffraction peak at 1.33 Å^{-1} due to repeated 4.7 Å spacing between β-strands in β-sheets.[46] (E) Protein diffraction peak area after 6 h of protein incubation. Full GIXD fit parameters and calculated values are reported in Table S5. Error bars in panels (C,E) are the parameter errors obtained from fitting.

accelerating binding and nucleating β-sheet formation after 6 h of incubation.[11] Overall, the purpose of these experiments was to determine how curcumin affected the binding of Aβ to an anionic membrane.

Curcumin Binds a DMPG Monolayer and Causes Lipid Tail Disorder. XR and GIXD measurements were first collected from a lipid monolayer made of pure DMPG. The measured reflectivity was normalized to the ideal interface Fresnel reflectivity (R/R_F) and plotted as a function of the scattering vector (q_z) to highlight deviations caused by electron-dense material present at the air/water interface (Figure S1A). The reflectivity data were fit to construct a model of electron density (ρ) as a function of depth along the z axis, normal to the membrane. We used a model-dependent fitting approach with distinct layers of electron density to represent different chemical moieties in the membrane. For example, the lipid tails, lipid heads, and water subphases were each represented with a unique component in the model. Each layer was parametrized with a value for electron density (reported normalized to water, ρ/ρ_{water}), thickness, and an interfacial roughness for smoothing between layers. The results of XR fitting were used to build a profile of electron density along z, moving from the air to the lipid tails, then headgroups, and finally to the aqueous subphase beneath the membrane. The overall DMPG electron density profile (black trace) is shown in Figure 2A, with a cartoon lipid overlaid as a guide. The exact parameters used to construct the electron density profile are shown in Figure 2B,C and Table S2. For pure DMPG, the lipid tails were 16 Å in length with ρ/ρ_{water} = 0.98 ± 0.02 and the headgroups were 9 Å in length with ρ/ρ_{water} = 1.57 ± 0.02. To ensure rigor in the fitting, each XR data set was also fit using a model-independent method. Results of this additional fitting are shown in Figure S2.

Curcumin was then injected into the subphase and allowed to interact with the DMPG monolayer. Data was collected after 0.5 and 2 h of curcumin incubation (Figures 2, S1A and Table S2). Curcumin caused a noticeable decrease in the lipid tail length (Figure 2B), suggesting a thinner and more disordered membrane. Curcumin also caused broadening of the lipid headgroup and decreased headgroup ρ/ρ_{water} (Figure 2C), consistent with curcumin embedding into the membrane to bind beneath the headgroups. XR measures an average of all molecules in the path of the X-ray beam; therefore, as curcumin embeds into the lipid headgroups, the data will represent an average electron density that is in-between that of a pure lipid headgroup and pure curcumin. The membrane thinning and reduction in electron density were moderate at 0.5 h of curcumin incubation, but they became more exaggerated after 2 h.

GIXD was used to detect the presence of semicrystalline ordered species in the membrane, specifically the amount of LC phase lipids under different conditions. From the fitted position of the integrated diffraction peak, the lattice spacing of the ordered species can be calculated ($d = 2\pi/q_{xy}$). From the pure DMPG membrane, a single diffraction peak was observed at q_{xy} = 1.49 Å^{-1} (Figure 2D and Table S5). This corresponds to an intermolecule spacing of 4.9 Å, assuming hexagonally packed lipid tails. The diffraction peak area is proportional to the relative amount of ordered material in the sample. After 0.5 h of interaction with curcumin, the area of the diffraction peak was reduced, indicating that some of the lipids had been converted from the LC phase to a disordered LE phase. No diffraction peak was detected after 2 h of curcumin incubation,

https://doi.org/10.1021/acschemneuro.3c00512
ACS Chem. Neurosci. 2023, 14, 4026−4038

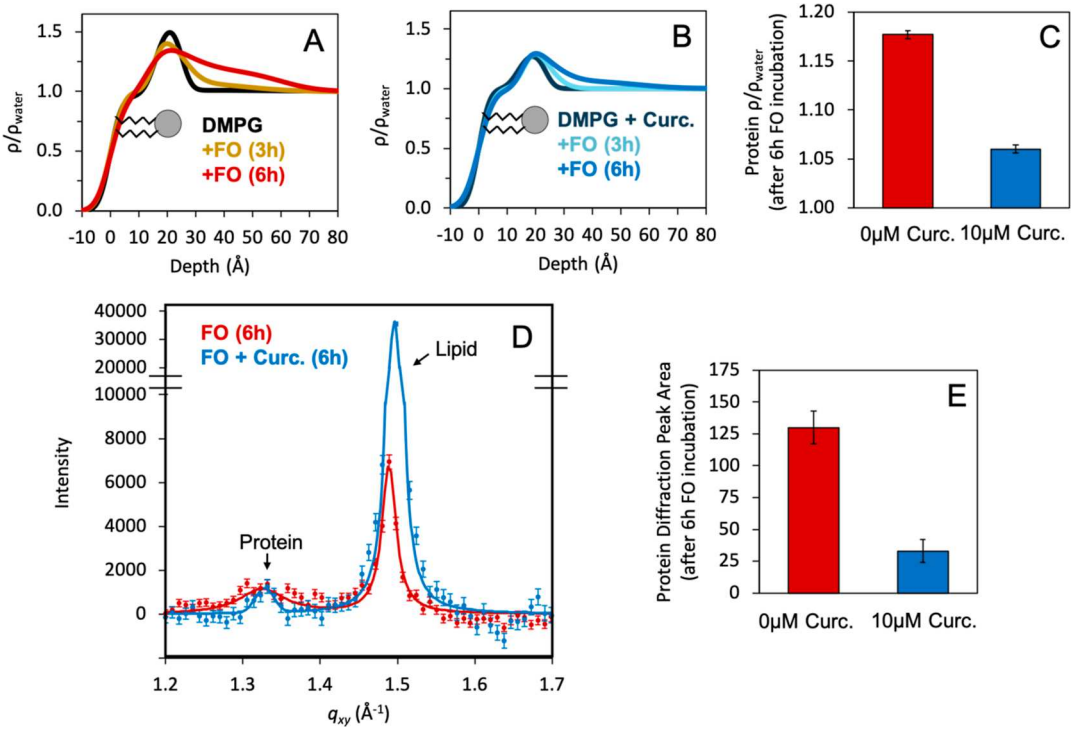

Figure 4. Curcumin reduces FO binding on a DMPG membrane. XR and GIXD data were collected from a pure DMPG monolayer (A) or a monolayer incubated with 10 μM curcumin for 2 h (B). FO was injected to reach a 2.5 μM subphase concentration, and data was collected after 3 and 6 h of incubation. (A,B) Normalized electron density profiles (ρ/ρ_{water}) are plotted as a function of depth along z, normal to the air/water interface. A cartoon lipid is overlaid onto the electron density profile. Reflectivity fits are shown in Figure S1D,E, and XR fit parameters are in Table S4. (C) Protein ρ/ρ_{water} parameters were from the model-dependent fitting of the XR data. (D) Background-subtracted GIXD data are shown as points with experimental error, and the peak fits are overlaid as lines. Amyloids produce a characteristic diffraction peak at 1.33 Å^{-1} due to repeated 4.7 Å spacing between β-strands in β-sheets.[46] (E) Protein diffraction peak area after 6 h of protein incubation. Full GIXD fit parameters and calculated values are reported in Table S5. Error bars in panels (C,E) are the parameter errors obtained from fitting.

indicating none of the lipids remained in the LC phase and the membrane had been completely converted to the disordered LE phase (Figure 2E).

Altogether, our results using an anionic lipid monolayer agree with previous findings for curcumin interacting with lipid bilayers. Previous studies have shown that curcumin embeds into membranes to rest between the lipid headgroups and the tails. Embedded curcumin also made the membrane more disordered and thinner. This preliminary work was important to determine what impact curcumin had on the DMPG monolayer in preparation for understanding Aβ interactions.

Curcumin Reduces Aβ_m and FO Binding to a DMPG Monolayer. After determining curcumin's impact on the DMPG monolayer, we next examined how the altered membrane structure would impact Aβ's membrane interactions and fibrillation. First, Aβ_m interactions with a pure DMPG membrane were tested in the absence of curcumin, and data was collected after 3 and 6 h of incubation. The electron density profile reveals an additional layer of electron-dense material beneath the lipid headgroups after 6 h of incubation with Aβ_m (Figures 3A and S1B). This layer of protein was ∼34 Å long, with ρ/ρ_{water} = 1.15 ± 0.01 (Table S3). For a homogeneous protein layer completely excluding solvent, a ρ/ρ_{water} of 1.23 is expected.[45] From a rough estimate based on a simple ratio of electron densities (0.15/0.23), Aβ covers ∼65% of the membrane surface. Aβ_m also caused a decrease in the headgroup ρ/ρ_{water}, suggesting the peptide is also embedding into the lipid monolayer.

In addition to the lipid diffraction peak from the DMPG tails at q_{xy} = 1.49 Å^{-1}, this sample also produced a protein diffraction peak at q_{xy} = 1.33 Å^{-1} (Figure 3D and Table S5). This q_{xy} position corresponds to a lattice spacing of 4.7 Å, which is the space between β-strands in a β-sheet. Fiber diffraction at 4.7 Å has been measured from studies on full-length amyloid fibrils,[46] thus the presence of this peak suggests that Aβ_m has assembled into β-sheet-rich structures at the membrane surface.

When curcumin was allowed to preincubate with the membrane for 2 h prior to Aβ_m injection, there was decreased Aβ accumulation at the membrane (Figure 3B,C). The electron density of the protein layer at 6 h was significantly reduced, showing only ∼26% coverage of the membrane surface. Interestingly, no protein diffraction peak was observed (Figure 3D,E), suggesting that although a small amount of Aβ_m was binding the membrane, it was not assembling into β-sheet-rich structures. Altogether, curcumin's impacts on membrane structure appear to cause a significant reduction of Aβ_m binding and assembly into β-sheet-rich structures.

Next, we examined the impact of curcumin on interactions between preformed FOs and DMPG. In the absence of curcumin, FO interacted with the pure DMPG monolayer and formed a ∼34 Å protein layer bound beneath the lipid headgroups (Figures 4A, S1 and Table S4). This protein layer had ρ/ρ_{water} = 1.177 ± 0.004, roughly equivalent to ∼77% membrane coverage. There were a few key differences between the FO and Aβ_m binding in the absence of curcumin. Specifically, FO bound the membrane faster than Aβ_m, with

https://doi.org/10.1021/acschemneuro.3c00512
ACS Chem. Neurosci. 2023, 14, 4026−4038

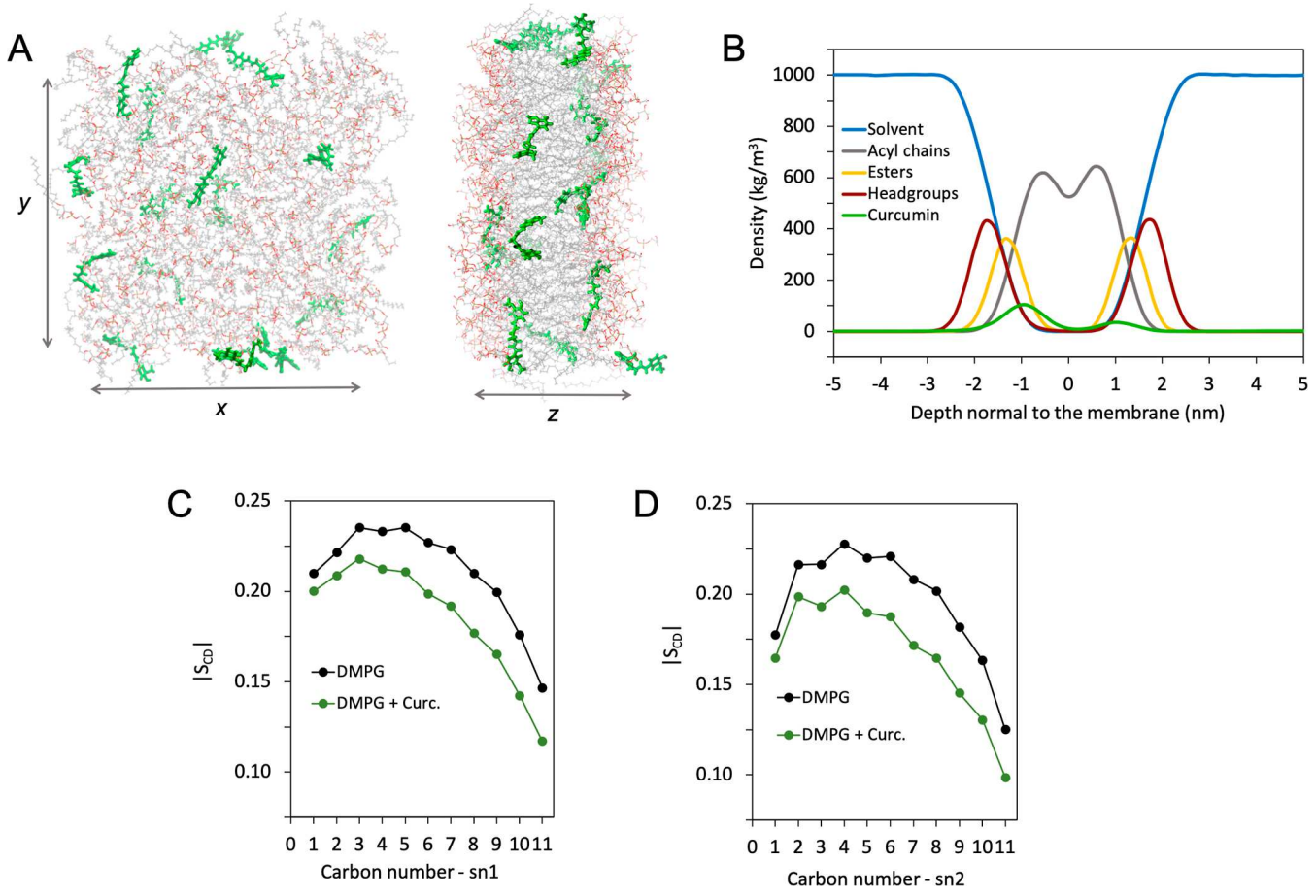

Figure 5. Curcumin is distributed beneath lipid headgroups and reduces lipid tail ordering. (A) Top-down and side views of a DMPG membrane containing 18 pre-embedded curcumin molecules (green) after 500 ns of simulation. (B) Calculated density of each chemical moiety plotted as a function of the depth normal to the membrane, with zero as the center of the lipid bilayer. (C,D) Calculated deuterium order parameter values for sn1 (E) and sn2 (F) lipid tails for a pure DMPG membrane with curcumin embedded. Plots show the results during the last 100 ns of the simulation, averaged between duplicate simulations.

a detectable protein layer accumulating beneath the membrane after 3 h. FO at 6 h also had a protein diffraction peak area that was approximately double that observed from Aβ_m at 6 h, suggesting twice the amount of β-sheet-rich structures accumulated at the membrane (Figures 3 and 4).

When curcumin was preincubated with the membrane for 2 h, it reduced the electron density of the FO layer bound beneath the membrane to ρ/ρ_{water} = 1.06 ± 0.01 (Figure 4B,C), equivalent to only ~26% membrane coverage. The area of the protein diffraction peak was also significantly reduced (Figure 4D,E and Table S5), corroborating that fewer β-sheet-rich structures were bound to the membrane.

Another interesting feature of these data is the dramatic increase in the lipid diffraction peak area when both curcumin and FO were present (Figure 4D), compared to the addition of either FO or curcumin. While the presence of either FO or curcumin reduced lipid tail order, the combination of both FO and curcumin restored the lipid diffraction to a similar level as pure DMPG. This was initially surprising, but it was corroborated by the lipid tail length also extending when FO and curcumin were both present in the membrane (15.3 Å), similar to the original length of the tails in the pure DMPG membrane (16.0 Å). By comparison, the length of the DMPG tails in the presence of curcumin was 13.8 Å, and FO was 13.3 Å. This may be explained by curcumin having preferential binding to FO over the DMPG, where curcumin could be condensing around the protein and decreasing the concentration of free curcumin dissolved in the membrane.

Curcumin Increases Lipid Tail Dynamics in Simulations. To complement the in vitro experimental data, we chose to perform MD simulations to better understand the molecular details of interactions of curcumin with Aβ in a membrane. Due to time-scale limitations, we did not attempt to observe de novo Aβ fibrillation at the membrane surface. Instead, we chose to simulate a preformed β-sheet-rich structure (similar to FOs) interacting with the membrane. The FO structure was determined experimentally (PDB 2LMN), and the OPM server was used to provide a starting model of FO bound to the membrane. The FO structure was predicted to span across both leaflets of the membrane (Figure S3C). We chose not to restrict FO interactions to one leaflet of the membrane, as this would be a very artificial limitation put in place just to align with our model membrane experimental system. Therefore, it is likely that in an actual membrane, FOs are both embedded into the membrane and also assembled into a β-sheet protein layer adhered to the membrane surface.

Curcumin was pre-embedded into the membrane near the lipid ester groups, a location supported by previous publications using both MD simulations and experimental methods.[44,47] We first performed an independent simulation

https://doi.org/10.1021/acschemneuro.3c00512
ACS Chem. Neurosci. 2023, 14, 4026−4038

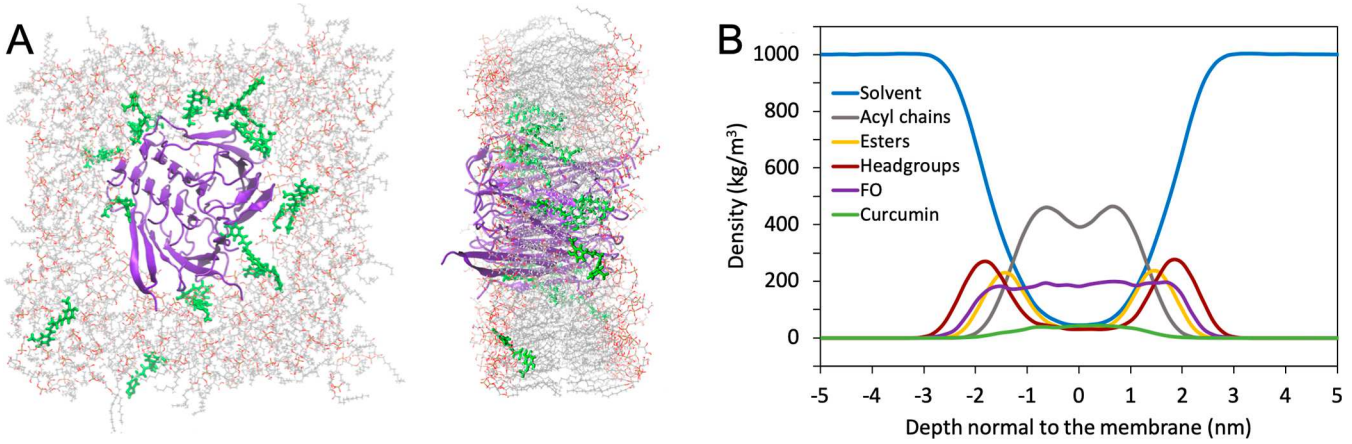

Figure 6. Curcumin clusters around FO when embedded in a membrane. (A) Top-down and side views of a DMPG membrane containing FO (purple) and curcumin (green) after 500 ns of simulation. (B) Calculated density of each chemical moiety plotted as a function of the depth normal to the membrane, with zero as the center of the lipid bilayer. The plot shows the results during the last 100 ns of the simulation, averaged between duplicate simulations.

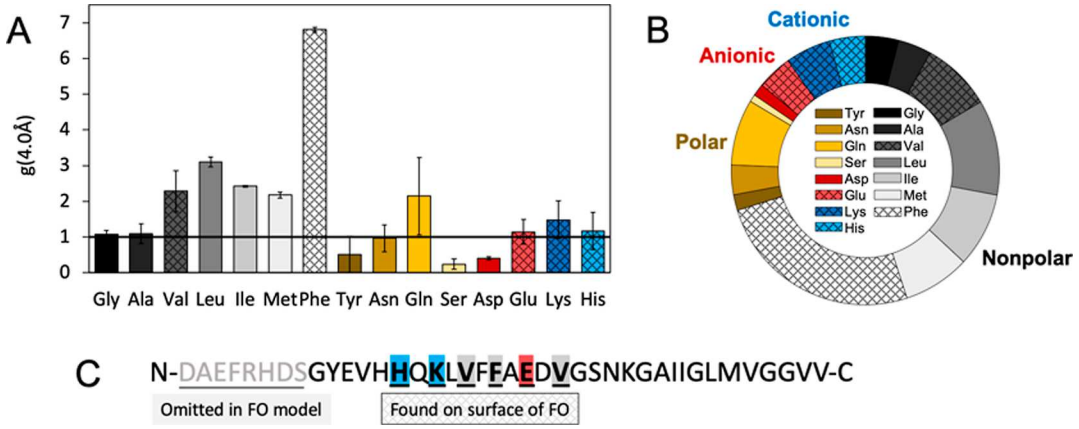

Figure 7. Curcumin preferentially interacts with Phe in the FO structure. (A) RDF describing interactions between each amino acid in FO and any curcumin molecule 4 Å away. Pair correlation function $g(r)$ outputs are normalized to the probability of observing the curcumin 45 Å away from the amino acid (horizontal line drawn at 1). For example, a value of 2 indicates that curcumin is twice as likely to be observed 4 Å away from an amino acid compared to being observed 45 Å away. For each RDF, $g(r)$ is also normalized to the number of atoms in that amino acid and the number of times that amino acid appears in the FO sequence. Amino acids are colored according to their interaction properties: nonpolar (grayscale), polar (yellows), anionic (reds), and cationic (blues). Grid patterns are overlaid to indicate the amino acids that appear with a high frequency on the surface of the FO structure. Data was calculated from the last 100 ns of each production, averaged between duplicate simulations. Error bars represent the full range of g (4.0 Å) values observed for each unaveraged simulation. Full RDF plots for all interaction distances are shown in Figure S5. (B) Pie chart of curcumin interactions with FO, with each amino acid representing a fraction of all interactions between FO and a curcumin molecule 4.0 Å away. (C) Aβ 1−40 sequence. The first 8 amino acids were omitted in the FO model because they were not resolved in the original experimental structure (PDB 2LMN). The amino acids H, K, V, F, and E are highlighted because they appear on the FO surface at high frequency, suggesting that curcumin is statistically more likely to interact with these amino acids.

with curcumin placed in the aqueous phase above the membrane, and indeed, curcumin did embed itself into the membrane (data not shown), in agreement with the previous literature. Therefore, we chose to start with the pre-embedded curcumin to capture interactions that would be occurring after the curcumin had equilibrated with the membrane.

After 500 ns, the curcumin remained distributed throughout the $x-y$ plane of the membrane, and the majority of the curcumin molecules (15/18) remained embedded in the membrane (Figure 5A). Partial density analysis (Figure 5B) revealed that indeed, curcumin remained primarily associated with the lipid esters, nestled between the headgroups and the acyl tails. Results from deuterium order parameter calculations showed that the lipid tails became more disordered when the curcumin was embedded into the membrane (Figure 5C,D). Overall, these simulation predictions agree with our X-ray scattering results (Figure S4) and the previously published work (both experimental and simulation) on the interactions of curcumin with membranes.

Curcumin Binds to Phe in Membrane-Embedded FO. Next, we examined interactions between curcumin and FO in a DMPG bilayer. In simulations containing only FO and DMPG, the protein remained relatively stationary over the course of the 500 ns simulation (Figure S3), suggesting the original OPM-predicted coordinates placed FO into a relatively stable interaction with the membrane. When FO was simulated in a membrane containing pre-embedded curcumin, several interesting changes occurred. After 500 ns of simulation, curcumin was no longer distributed throughout the membrane but instead was clustered around the FO (Figure 6A). The changes

https://doi.org/10.1021/acschemneuro.3c00512
ACS Chem. Neurosci. 2023, 14, 4026−4038

in curcumin distribution are also noticeable from the partial density plot (Figure 6B), which shows that curcumin was no longer localized near the lipid esters and had moved to clusters near the membrane center.

To identify what interactions were driving curcumin to cluster around FO, we performed radial distribution function (RDF) calculations to determine which amino acids were within the interaction distance (4.0 Å) of curcumin during the final 100 ns of simulation (Figure 7A,B). Interaction probabilities across all distances are shown in Figure S5. Data was normalized for residue size and number of occurrences in the FO sequence, where a value of 1 is equal to the probability of finding a curcumin molecule 45 Å away from that residue, essentially equivalent to no preferential contacts with that residue. Curcumin generally interacted the most with nonpolar residues, specifically favoring phenylalanine. This FO structure has His, Lys, Val, Phe, and Glu side chains found on the surface pointed toward the DMPG lipid tails; therefore, curcumin is statistically more likely to form interactions with these residues compared to residue buried in the FO interior (Figures 7C and S6). Curcumin also had favorable interactions with Leu, Ile, Met, and Gln residues, which are accessible through interactions with the β-strands that form the edges of the FO along the fibril growth axis. Examining the interactions between curcumin and Phe, curcumin appears to form disorganized clusters around exposed Phe side chains (Figure S7). $\pi-\pi$ stacking was occasionally observed with Phe side chains at the end of the FO structure; however, curcumin did not embed between Phe side chains to displace previously existing Phe−Phe interactions. Interestingly, curcumin interactions caused a slight decrease in β-sheets and turns while also increasing the random coil content in the FOs (−3% β-sheets, −7% turns, and +8% random coil). This suggests that curcumin may be destabilizing the classic β-sheet-rich oligomer conformation typically associated with amyloid protein misfolding.

Summary and Perspective. Overall, we have observed that curcumin reduces β-sheet-rich Aβ oligomers binding to an anionic model membrane. Our findings from X-ray scattering experiments and MD simulations were consistent with previous results showing that curcumin embeds into a lipid membrane and causes membrane thinning and lipid tail disorganization. This altered membrane structure appears to reduce both $A\beta_m$ and FO binding beneath the membrane, as evidenced by both reduced electron density of the protein layer and decreased diffraction from β-sheet-rich protein species. Simulations containing a DMPG lipid bilayer, curcumin, and membrane-embedded FO showed that curcumin clusters around the FO, forming favorable contacts with exposed phenylalanine side chains. Overall, curcumin likely reduced the extent of interactions of FO with membranes through both altering the membrane structure and favorable binding to the FO surface.

GIXD results showed that curcumin and FO individually caused tail disorganization in the DMPG monolayer, as shown by reduced lipid diffraction peak areas. Interestingly, the combination of both curcumin and FO restored DMPG tail diffraction to a level near the pure DMPG membrane, suggesting that the lipids returned to an LC-ordered state. This result may be explained by the MD simulations showing curcumin clustered around the FO, no longer homogeneously distributed throughout the membrane. Curcumin may favor FO interactions over lipid interactions; therefore, clustering around the FO may be decreasing the relative concentration of curcumin solubilized in the membrane.

Aβ causes toxic membrane thinning and pore formation; therefore, curcumin's ability to disrupt Aβ binding and aggregation could be a route of interest in further AD studies. However, another facet that should be addressed is the impact of membrane thinning caused by curcumin itself. Curcumin is a hydrophobic molecule with intrinsic amphipathicity; therefore, the cellular impacts of potentially deleterious membrane structure perturbation should be examined, especially in combination with damaging membrane thinning caused by Aβ. Curcumin thins lipid bilayers and decreases their stiffness,[47−51] and one report showed that curcumin disrupted a lipid bilayer and induced the formation of micelles, transmembrane pores, and toroidal pores.[52] Curcumin also induces leakage from unilamellar liposomes, dependent on cholesterol concentration.[48]

Another remaining question is what impact curcumin would have on membrane interactions with Aβ oligomers that have a globular (not β-sheet-rich) structure. It is generally agreed that Aβ oligomers are the most neurotoxic structures; however, the distinction between β-sheet-rich FOs and nonfibrillar oligomers is not always made clear in the literature. Nonfibrillar oligomers have been found to disrupt membrane integrity through a detergent-like effect,[53] suggesting an important opportunity for curcumin interactions with the surface-exposed hydrophobic patches that give these Aβ oligomers their high toxicity. The work presented in this study only addressed FOs, as such the unique detergent-like effect of nonfibrillar oligomers should also be investigated in future work concerning curcumin, Aβ oligomers, and membranes.

Overall, we find that curcumin reduces interactions between amyloidogenic Aβ oligomers and anionic membranes, and this effect is likely driven by a combination of curcumin's impact on membrane structure and its affinity for the Aβ oligomer surface. In the future, it will also be interesting to explore the impact of other small polyphenolic molecules, such as resveratrol, myricetin, and rosmarinic acid, as some of these molecules have shown to be more effective at inhibiting Aβ aggregation in an aqueous environment.[54,55] This phenomenon of amyloidogenic peptides forming favorable interactions with negatively charged membranes is prevalent in several neurodegenerative diseases. Aβ interacts with gangliosides on the outer leaflet of neuronal membranes,[17,56,57] tau interacts with anionic lipids on the cytoplasmic-facing leaflet of the nuclear envelope,[13,58] and α-synuclein interacts with phosphatidylserine lipids on synaptic vesicles.[59] Additional studies are required to determine whether the data obtained from this simplified model system may be representative of broader amyloidogenic protein interactions with biological membrane surfaces. Although pharmaceutical AD treatment with curcumin has major challenges, this work helps build foundational knowledge about the interactions of the Aβ oligomer with anionic membranes and how this could potentially be mitigated.

METHODS

Materials. Lyophilized $A\beta_{1-40}$ powder was obtained from Peptide 2.0 (Chantilly, VA) with 95.49% purity (purified by reverse-phase HPLC). DMPG was purchased from Avanti Polar Lipids (Alabaster, AL) as a dry powder. DMPG stock solution was prepared at 3.0 mg/mL in 7:3 v/v chloroform to methanol. For use during Langmuir trough assays, the stock was diluted to a 0.2 mg/mL spreading

https://doi.org/10.1021/acschemneuro.3c00512
ACS Chem. Neurosci. 2023, 14, 4026−4038

solution and was stored at −20 °C. Lipid solutions were vortexed and sonicated for 30 s prior to each use. Curcumin (a mixture of curcumin, demethoxycurcumin, and bisdemethoxycurcumin) was obtained from Acros Organics (Morris Plains, New Jersey) at 98% purity. Curcumin stock was prepared at 30 mM in dimethyl sulfoxide and stored in a −20 °C freezer. The curcumin solution was protected from light to reduce photodegradation.

There were no unexpected, new, or significant hazards or risks associated with the reported work.

Preparation of Monomeric Aβ and Fibrillar Oligomers. $A\beta_m$ was prepared by solubilizing lyophilized Aβ 1−40 peptide in 100% DMSO at 2 mg/mL. The solution was sonicated for 30 s and then centrifuged for 10 min at 14,000 rpm to remove insoluble aggregates. The supernatant was collected and aliquoted to avoid freeze−thaw cycles. The aliquots were stored at −80 °C. Immediately prior to use, the DMSO-solubilized monomeric Aβ was diluted to desired concentrations with 18 MΩ water.

FO preparation followed a protocol adapted from Breydo et al.[60] FOs were prepared by dissolving 0.3 mg of lyophilized Aβ 1−40 into 180 μL of hexafluoroisopropanol and incubating at room temperature for 25 min. The solution was diluted to a total volume of 1060 μL with 18 MΩ water. The solution was stirred in an open microcentrifuge tube for 6−8 h at room temperature. To remove HFIP from the solution, a stream of N_2 was blown over the sample until it reached ∼1/3 of the original volume, then water was added to return the sample to its original volume. The FOs were then centrifuged for 10 min at 14,000 rpm. The supernatant was then collected, aliquoted, and stored at −80 °C. $A\beta_m$ and FO peptide concentrations were determined by UV/vis absorbance via Nanodrop with an Aβ extinction coefficient of 1490 M^{-1} cm^{-1} at 280 nm.

Fourier Transform Infrared Spectroscopy. FTIR was used to determine protein secondary structure and confirm the successful preparation of $A\beta_m$ and FO through analysis of the amide I bands in the 1600−1700 cm^{-1} range. Data were collected using a Thermo Scientific FTIR Spectrometer (model Is5) with OMNIC Spectra software for data collection, processing, and peak identification. 2−4 μL of $A\beta_m$ or FO solution was placed on the FTIR crystal, and the solvent was allowed to evaporate off for 20 min prior to data collection. Three replicated scans were collected. Each resulting spectrum was baseline corrected and background subtracted.

X-ray Reflectivity and Grazing Incidence X-ray Diffraction Data Collection. Two liquid surface X-ray scattering methods were used: XR and GIXD. These methods were used to determine structural details about Aβ interactions with a lipid monolayer, namely, detecting diffracting species and determining a profile of electron density normal to the monolayer. XR and GIXD experiments were performed at the Advanced Photon Source (APS) at Argonne National Laboratories (Sector 15 NSF's ChemMatCARS) with synchrotron X-rays. A 20 mL PTFE Langmuir trough (6.5 × 6.5 cm^2) was filled with degassed water, and experiments were performed with a constant trough area at room temperature (23.5 ± 0.5 °C). Surface pressure was monitored with a Wilhelmy plate balance (KSV Instruments, Finland). A DMPG monolayer was assembled at the air/water interface at a surface pressure of 25 mN/m. The membrane was left undisturbed for 20 min to allow for chloroform evaporation and equilibration of the membrane structure.

For experiments containing only DMPG and 10 μM curcumin, XR and GIXD data were collected at 30 min and 2 h after curcumin injection into the subphase. For experiments with 2.5 μM $A\beta_m$ or FO, XR and GIXD data were collected at 3 and 6 h after protein injection into the subphase. Surface pressure measurements were used to detect when protein binding had plateaued, as surface pressure increases are expected when proteins bind the membrane. For experiments containing both curcumin and $A\beta_m$/FO, the 2 h curcumin incubation was completed, then the $A\beta_m$ or FO was injected into the subphase, and data was collected 3 and 6 h after protein injection. Duplicate XR and GIXD measurements were made on each sample while peptide insertion was equilibrated. For all experiments, the trough was sealed in a canister, and the air inside was purged with helium gas. Data collection proceeded after the oxygen content was <2% to prevent background scattering and oxidative beam damage to the monolayer. Data was collected using X-rays with a wavelength of 1.24 Å, and the dimensions of the incoming X-ray beam footprint on the liquid surface were ∼1 × 3−10 mm^2 for XR and ∼1 × 29 mm^2 for GIXD. The data were collected by tilting a germanium monochromator crystal to deflect the beam and change the angle of incidence on the sample. Intensities were collected, background subtracted, and normalized to the incident beam flux. For XR, intensities were collected over the range $0.016 < q_z < 0.8$ $Å^{-1}$. For GIXD, an incident beam struck the water surface at momentum transfer vector $q_z = 0.85 \times q_c$, where $q_c = 0.02176$ $Å^{-1}$ is the critical scattering vector for total external reflection from the subphase. At this q_z, an evanescent wave is generated that travels along the surface and can Bragg scatter from molecular arrangements at the surface. Each data collection scan typically required 1 h; as an additional precaution against beam damage, the trough was systematically translated by 1 mm (horizontally) during data collection. The data presented is from one single scan; however, the data was found to be reproducible when the samples were repeatedly scanned. A subset of experiments was performed in duplicate, and the duplicate measurements were found to be reproducible. X-ray scattering was detected with a Dectris PILATUS 100 K detector, and XR and diffraction images were integrated using Python software developed by APS beamline scientist Wei Bu (https://github.com/weibu/Liquid_Surface_ChemMatCARS).

X-ray Reflectivity Theory and Data Analysis. XR was used to measure the electron density of materials deposited at the air−water interface on a Langmuir trough, including the lipid monolayer and any bound protein. This method can be used to detect protein binding to a membrane and determine the resulting changes to membrane structure. If the protein is adsorbing onto the membrane through interactions with lipid headgroups, this can be observed as an increase in electron density beneath the lipid tails. If protein or small molecule interactions with the lipids cause changes to the membrane structure, there will be changes in the electron density and length of the lipid tails and headgroups. X-ray scattering theory has been fully described previously,[61−64] and only a summary is provided here. By measuring the intensity of reflected X-rays, one can deduce detailed information about the electron density distribution normal to the interface, $\rho(z)$, laterally averaged over both the ordered and disordered parts of the film. The reflectivity is defined as the ratio of reflected to incident beam intensities, in a specular geometry, as a function of the vertical momentum transfer vector $q_z = (4\pi/\lambda) \sin(\theta)$, where θ is the incident angle of the X-ray on the surface. Finally, the reflectivity curve can be analyzed to obtain the in-plane averaged electron density distribution normal to the interface.

The reflectivity data are presented after division by the Fresnel reflectivity (scattering from an infinitely sharp air−water interface) (R_F), with error bars representing one standard deviation error for each data point. Division by Fresnel reflectivity provided better visualization of the XR data. A model-dependent fitting method was used to fit the XR data, where a discrete layer model was used to obtain the electron density profile normal to the interface. The studied system was divided into layers with parameters for thickness, electron density, and an interfacial roughness approximated by error functions. The parameters of this model were adjusted using program Motofit[65] in IgorPro to obtain lowest χ^2 values and reasonable values of the parameters. Parameter uncertainties were estimated using a finite difference approach with a covariance matrix describing the concavity of χ^2 with respect to each fit parameter. However, due to the interdependence of the parameters, we expect that parameter errors may be underestimated in the reported data. For rigor and reproducibility in the data fitting, the data were also analyzed using a model-independent approach based on cubic B-splines to obtain the electron density profile normal to the interface.[66] The coefficients in the B-spline series were determined by constrained nonlinear least-squares methods, in which the smoothest solution with the lowest χ^2 goodness of fit was chosen. Over several thousand refinements were performed within the parameter space, and a family of models is

https://doi.org/10.1021/acschemneuro.3c00512
ACS Chem. Neurosci. 2023, 14, 4026−4038

presented for each reflectivity data set, all of which satisfy $\chi^2 < \chi^2_{min} + 20\%$ with typical values of $\chi^2_{min} < 10$.[67]

Grazing Incidence X-ray Diffraction Theory and Data Analysis. GIXD was used to detect the presence of diffracting species at the air/water interface. This data can be analyzed to quantify the lattice spacing (d) between ordered molecules, the approximate size of crystallites, and the relative amount of material packed into semicrystalline structures at the air/water interface. For this particular system, we expected to observe diffraction from lipid tails arranged in a LC phase and Aβ peptides arranged into β-sheet-rich structures.[14] GIXD is performed by using an X-ray beam striking the membrane at a thin angle to generate an evanescent wave that can Bragg scatter from crystallites on the membrane surface. For these experiments, the diffraction angle is expressed in terms of a scattering vector (q_{xy}) that is related to d via the relationship $d = 2\pi/q_{xy}$, where q_{xy} is the position of the diffraction peak, as determined from a Lorentzian fit to the background-subtracted diffraction data. The diffraction peak area is correlated to the relative amount of diffracting material. The coherence length (L_c), or average size of diffracting crystallites, can be calculated from the full width half-maximum (fwhm) of the diffraction peak using the Scherrer formula, $L_c = (0.9 \times 2\pi)/(\text{fwhm}^2 - 0.006^2)^{1/2}$.[68] The q_{xy} resolution of the ChemMatCARS liquid surface instrument, $\Delta q_{xy} = 0.006$ Å^{-1}, was taken into consideration to calculate the intrinsic fwhm values. Background-subtracted GIXD peaks were fit by using the MultiPeak Fit 2.0 function in IgorPro.

Molecular Dynamics Simulations. CHARMM-GUI[69] was used to build each of the systems. The pure membrane system was built with 202 DMPG molecules and 12079 TIP3 molecules in a rectangular box with dimensions of 7.9 nm × 7.9 nm × 9.1 nm, forming a water layer 3.5 nm thick. To embed curcumin into the membrane, 18 curcumin molecules were placed in a variety of orientations in a grid-like pattern, with 9 curcumin molecules in each leaflet of the membrane. The curcumin molecules were placed at the height of the lipid esters, following previously published literature.[70] Lipids were packed around the curcumin molecules using the InflateGro script.[71] The coordinates for FO were obtained from PDB 2LMN,[72] and OPM was used to predict protein insertion into the membrane. For FO bound to a DMPG membrane with embedded curcumin, a single coordinate file was made containing the curcumin molecules and the FO, and then the InflateGro script was used to pack the lipids around these molecules. Curcumin molecules that overlapped with the FO coordinates were deleted, leaving 16 curcumin molecules in the system. For the FO system, the water layer was 50 Å thick on each side of the membrane to accommodate the portions of the FO that protruded out of the membrane. Each system was built with 0.1 M NaCl in the solvent, with additional ions added to neutralize the overall system charge. Table S1 summarizes the number of lipids, water molecules, and box dimensions for each system.

The systems were parametrized with the CHARMM c36m force field,[73] and simulations were performed using GROMACS 2021.4.[74] Curcumin was parametrized using the CHARMM general force field (CGENFF).[75] These parameters have been previously validated and found to accurately model curcumin's behavior.[70] For all simulations, minimization was performed by steepest descent until the maximum force was less than 1000 kJ/(mol nm). For membrane-only systems, equilibration was performed in six parts, each lasting 25 ps. Equilibration began with a force constant of 1000 kJ/(mol nm^2) to restrain the lipids and was gradually reduced throughout the equilibration. For systems containing protein, a longer equilibration was performed over 6 steps of 125, 125, 125, 250, 250, and 250 ps each, with a 4000 kJ/(mol nm^2) restraint on the protein backbone and a 2000 kJ/(mol nm^2) restraint on the protein side chains, in addition to the lipid restraints. All restraints were gradually reduced throughout the equilibration. The temperature was maintained at 303.15 K using the Berendsen thermostat, and pressure was controlled using the Berendsen semi-isotropic barostat. Long-range electrostatics were calculated using the particle-mesh Ewald summation, and a Verlet cutoff scheme was applied with a 1.2 nm distance for all nonbonding interactions. Bonds were constrained using LINCS. During production, the temperature and pressure were controlled with a Nose–Hoover and semi-isotropic Parrinello–Rahman thermostat and barostat, respectively. Simulations were performed using 2 fs time steps.

Each system was simulated in duplicate 500 ns productions for a total of 1 μs of simulation. For deuterium order parameters, partial density analysis calculations, and RDF, the final 100 ns of the simulation was used, and the average of the data from the duplicate simulations is reported. The deuterium order parameters, density of each membrane component, and RDF were calculated using the GROMACS tools gmx order, density, and rdf, respectively. Visual MD was used to visualize trajectories and calculate predicted secondary structure content.[76]

■ ASSOCIATED CONTENT

Supporting Information

The Supporting Information is available free of charge at https://pubs.acs.org/doi/10.1021/acschemneuro.3c00512.

Additional background information, XR and GIXD fit parameters and fits, MD system build information, additional MD simulations, additional MD analysis. (PDF)

■ AUTHOR INFORMATION

Corresponding Author

Crystal M. Vander Zanden − *Department of Chemistry and Biochemistry, University of Colorado Colorado Springs, Colorado Springs, Colorado 80918, United States;* orcid.org/0000-0003-3248-6028; Email: cvanderz@uccs.edu

Authors

Chad A. Sallaberry − *Department of Chemistry and Biochemistry, University of Colorado Colorado Springs, Colorado Springs, Colorado 80918, United States*

Barbie J. Voss − *Department of Chemistry and Biochemistry, University of Colorado Colorado Springs, Colorado Springs, Colorado 80918, United States*

William B. Stone − *Department of Chemistry and Biochemistry, University of Colorado Colorado Springs, Colorado Springs, Colorado 80918, United States*

Fabiola Estrada − *Department of Chemistry and Biochemistry, University of Colorado Colorado Springs, Colorado Springs, Colorado 80918, United States*

Advita Bhatia − *Department of Chemistry and Biochemistry, University of Colorado Colorado Springs, Colorado Springs, Colorado 80918, United States*

J. Daniel Soto − *Department of Chemistry and Biochemistry, University of Colorado Colorado Springs, Colorado Springs, Colorado 80918, United States*

Charles W. Griffin − *Department of Chemistry and Biochemistry, University of Colorado Colorado Springs, Colorado Springs, Colorado 80918, United States*

Complete contact information is available at: https://pubs.acs.org/10.1021/acschemneuro.3c00512

Author Contributions

C.A.S., B.J.V., and W.B.S. are contributed equally to this work and share first authorship. C.S. and F.E. performed the X-ray scattering data collection and analysis. B.V., W.B.S., and A.B. performed the molecular dynamics simulations and analysis. J.S. and C.G. assisted with the manuscript preparation. C.V.Z. designed research and the original concept for the paper,

https://doi.org/10.1021/acschemneuro.3c00512
ACS Chem. Neurosci. 2023, 14, 4026−4038

performed additional data analysis, made the figures, and primarily wrote the manuscript. C.S., B.V., W.B.S., F.E., A.B., J.S., C.G., and C.V.Z. edited and revised the manuscript.

Funding

W.B.S. and A.B. were funded by the UCCS Undergraduate Research Academy.

Notes

The authors declare no competing financial interest.

■ ACKNOWLEDGMENTS

NSF's ChemMatCARS, Sector 15-ID-C at the Advanced Photon Source (APS), Argonne National Laboratory (ANL), is supported by the Divisions of Chemistry (CHE) and Materials Research (DMR), National Science Foundation, under grant number NSF/CHE- 1834750. This research used resources of the Advanced Photon Source, a U.S. Department of Energy (DOE) Office of Science user facility operated for the DOE Office of Science by Argonne National Laboratory under contract no. DE-AC02-06CH11357. The authors are grateful to beamline scientist Dr. Wei Bu for support during XR and GIXD data collection. Dr. Erik Watkins is acknowledged for generously sharing his software for model-independent fitting of XR data. This work used allocation number MBC180100 for the Extreme Science and Engineering Discovery Environment (XSEDE), which was supported by the National Science Foundation grant number ACI-1053575.

■ ABBREVIATIONS

DMPG, 1,2-dimyristoyl-*sn*-glycero-3-phosphorylglycerol; MD, molecular dynamics; RDF, radial distribution function; Aβ, amyloid beta; Aβ_m, amyloid beta monomer; FO, fibrillar oligomer; AD, Alzheimer's disease; XR, X-ray reflectivity; GIXD, grazing incidence X-ray diffraction; FTIR, Fourier transform infrared spectroscopy; R/R_F, reflectivity normalized to Fresnel reflectivity; LC, liquid condensed; LE, liquid expanded; fwhm, full-width half-maximum; L_c, coherence length; d, lattice spacing; OPM, Orientations of Proteins in Membranes

■ REFERENCES

(1) Benzinger, T. L. S.; Gregory, D. M.; Burkoth, T. S.; Miller-Auer, H.; Lynn, D. G.; Botto, R. E.; Meredith, S. C. Two-Dimensional Structure of β-Amyloid(10−35) Fibrils. *Biochemistry* **2000**, *39* (12), 3491−3499.

(2) Wälti, M. A.; Ravotti, F.; Arai, H.; Glabe, C. G.; Wall, J. S.; Böckmann, A.; Güntert, P.; Meier, B. H.; Riek, R. Atomic-Resolution Structure of a Disease-Relevant Aβ(1−42) Amyloid Fibril. *Proc. Natl. Acad. Sci. U.S.A.* **2016**, *113* (34), E4976−E4984.

(3) Selkoe, D. J. Physiological Production of the β-Amyloid Protein and the Mechanism of Alzheimer's Disease. *Trends Neurosci.* **1993**, *16* (10), 403−409.

(4) Soto, C. Unfolding the Role of Protein Misfolding in Neurodegenerative Diseases. *Nat. Rev. Neurosci.* **2003**, *4* (1), 49−60.

(5) Glabe, C. C. Amyloid Accumulation and Pathogenesis of Alzheimer's Disease: Significance of Monomeric, Oligomeric and Fibrillar Aβ. *Alzheimer's Disease*; *Subcellular Biochemistry*; Harris, J. R., Fahrenholz, F., Eds.; Springer: Boston, MA, 2012; Vol. *38*, pp 167−177.

(6) Kayed, R.; Head, E.; Thompson, J. L.; McIntire, T. M.; Milton, S. C.; Cotman, C. W.; Glabe, C. G. Common Structure of Soluble Amyloid Oligomers Implies Common Mechanism of Pathogenesis. *Science* **2003**, *300*, 486−489.

(7) Xue, W.; Hellewell, A. L.; Gosal, W. S.; Homans, S. W.; Hewitt, E. W.; Radford, S. E. Fibril Fragmentation Enhances Amyloid Cytotoxicity. *J. Biol. Chem.* **2009**, *284* (49), 34272−34282.

(8) Dahlgren, K. N.; Manelli, A. M.; Stine, W. B.; Baker, L. K.; Krafft, G. A.; Ladu, M. J. Oligomeric and Fibrillar Species of Amyloid-β Peptides Differentially Affect Neuronal Viability. *J. Biol. Chem.* **2002**, *277* (35), 32046−32053.

(9) Nirmalraj, P. N.; List, J.; Battacharya, S.; Howe, G.; Xu, L.; Thompson, D.; Mayer, M. Complete Aggregation Pathway of Amyloid β (1−40) and (1−42) Resolved on an Atomically Clean Interface. *Sci. Adv.* **2020**, *6*, No. eaaz6014.

(10) Fanni, A. M.; Vander Zanden, C. M.; Majewska, P. V.; Majewski, J.; Chi, E. Y. Membrane-Mediated Fibrillation and Toxicity of the Tau Hexapeptide PHF6. *J. Biol. Chem.* **2019**, *294* (42), 15304−15317.

(11) Vander Zanden, C. M.; Wampler, L.; Bowers, I.; Watkins, E. B.; Majewski, J.; Chi, E. Y. Fibrillar and Nonfibrillar Amyloid Beta Structures Drive Two Modes of Membrane-Mediated Toxicity. *Langmuir* **2019**, *35* (48), 16024−16036.

(12) Majewski, J. P.; Jones, E. M.; Vander Zanden, C. M.; Biernat, J.; Mandelkow, E.; Chi, E. Y. Lipid Membrane Templated Misfolding and Self-Assembly of Intrinsically Disordered Tau Protein. *Sci. Rep.* **2020**, *10*, 13324.

(13) Sallaberry, C. A.; Voss, B. J.; Majewski, J.; Biernat, J.; Mandelkow, E.; Chi, E. Y.; Vander Zanden, C. M. Tau and Membranes: Interactions That Promote Folding and Condensation. *Front. Cell Dev. Biol.* **2021**, *9*, 725241.

(14) Chi, E. Y.; Ege, C.; Winans, A.; Majewski, J.; Wu, G.; Kjaer, K.; Lee, K. Y. C. Lipid Membrane Templates the Ordering and Induces the Fibrillogenesis of Alzheimer's Disease Amyloid-β Peptide. *Proteins: Struct., Funct., Bioinf.* **2008**, *72* (1), 1−24.

(15) Jones, E. M.; Dubey, M.; Camp, P. J.; Vernon, B. C.; Biernat, J.; Mandelkow, E.; Majewski, J.; Chi, E. Y. Interaction of Tau Protein with Model Lipid Membranes Induces Tau Structural Compaction and Membrane Disruption. *Biochemistry* **2012**, *51* (12), 2539−2550.

(16) Williams, T. L.; Day, I. J.; Serpell, L. C. The Effect of Alzheimer's Aβ Aggregation State on the Permeation of Biomimetic Lipid Vesicles. *Langmuir* **2010**, *26* (22), 17260−17268.

(17) Chi, E. Y.; Frey, S. L.; Lee, K. Y. C. Ganglioside GM1-Mediated Amyloid-Beta Fibrillogenesis and Membrane Disruption. *Biochemistry* **2007**, *46*, 1913−1924.

(18) Zhao, H.; Tuominen, E. K. J.; Kinnunen, P. K. J. Formation of Amyloid Fibers Triggered by Phosphatidylserine-Containing Membranes. *Biochemistry* **2004**, *43*, 10302−10307.

(19) Robinson, J.; Sarangi, N. K.; Keyes, T. E. Role of Phosphatidylserine in Amyloid-Beta Oligomerization at Asymmetric Phospholipid Bilayers. *Phys. Chem. Chem. Phys.* **2023**, *25*, 7648−7661.

(20) Martín, V.; Fabelo, N.; Santpere, G.; Puig, B.; Marín, R.; Ferrer, I.; Díaz, M. Lipid Alterations in Lipid Rafts from Alzheimer's Disease Human Brain Cortex. *J. Alzheimer's Dis.* **2010**, *19* (2), 489−502.

(21) Fabiani, C.; Antollini, S. S. Alzheimer's Disease as a Membrane Disorder: Spatial Cross-Talk among Beta-Amyloid Peptides, Nicotinic Acetylcholine Receptors and Lipid Rafts. *Frontiers in Cellular Neuroscience*; Frontiers Media S.A., 2019.

(22) Hicks, D. A.; Nalivaeva, N. N.; Turner, A. J. Lipid Rafts and Alzheimer's Disease: Protein-Lipid Interactions and Perturbation of Signaling. *Front. Physiol.* **2012**, *3*, 189.

(23) Canale, C.; Seghezza, S.; Vilasi, S.; Carrotta, R.; Bulone, D.; Diaspro, A.; San Biagio, P. L.; Dante, S. Different Effects of Alzheimer's Peptide Aβ(1−40) Oligomers and Fibrils on Supported Lipid Membranes. *Biophys. Chem.* **2013**, *182*, 23−29.

(24) Sokolov, Y.; Kozak, J. A.; Kayed, R.; Chanturiya, A.; Glabe, C.; Hall, J. E. Soluble Amyloid Oligomers Increase Bilayer Conductance by Altering Dielectric Structure. *J. Gen. Physiol.* **2006**, *128* (6), 637−647.

(25) Dong, X.; Sun, Y.; Wei, G.; Nussinov, R.; Ma, B. Binding of Protofibrillar Aβ Trimers to Lipid Bilayer Surface Enhances Aβ Structural Stability and Causes Membrane Thinning. *Phys. Chem. Chem. Phys.* **2017**, *19*, 27556−27569.

https://doi.org/10.1021/acschemneuro.3c00512
ACS Chem. Neurosci. 2023, 14, 4026−4038

(26) Mari, S. A.; Wegmann, S.; Tepper, K.; Hyman, B. T.; Mandelkow, E. M.; Mandelkow, E.; Müller, D. J. Reversible Cation-Selective Attachment and Self-Assembly of Human Tau on Supported Brain Lipid Membranes. *Nano Lett.* **2018**, *18* (5), 3271−3281.
(27) Brekk, O. R.; Moskites, A.; Isacson, O.; Hallett, P. J. Lipid-Dependent Deposition of Alpha-Synuclein and Tau on Neuronal Secretogranin II-Positive Vesicular Membranes with Age. *Sci. Rep.* **2018**, *8* (1), 15207.
(28) Dicke, S. S.; Tatge, L.; Engen, P. E.; Culp, M.; Masterson, L. R. Isothermal Titration Calorimetry and Vesicle Leakage Assays Highlight the Differential Behaviors of Tau Repeat Segments upon Interaction with Anionic Lipid Membranes. *Biochem. Biophys. Res. Commun.* **2017**, *493* (4), 1504−1509.
(29) Galvagnion, C.; Buell, A. K.; Meisl, G.; Michaels, T. C. T.; Vendruscolo, M.; Knowles, T. P. J.; Dobson, C. M. Lipid vesicles trigger α-synuclein aggregation by stimulating primary nucleation. *Nat. Chem. Biol.* **2015**, *11* (3), 229−234.
(30) Prasad, S.; Aggarwal, B. B. Turmeric, the Golden Spice. *Herbal Medicine: Biomolecular and Clinical Aspects*, 2nd ed.; CRC Press, 2011.
(31) Yang, F.; Lim, G. P.; Begum, A. N.; Ubeda, O. J.; Simmons, M. R.; Ambegaokar, S. S.; Chen, P.; Kayed, R.; Glabe, C. G.; Frautschy, S. A.; Cole, G. M. Curcumin Inhibits Formation of Amyloid β Oligomers and Fibrils, Binds Plaques, and Reduces Amyloid in Vivo. *J. Biol. Chem.* **2005**, *280* (7), 5892−5901.
(32) Ausili, A.; Gómez-Murcia, V.; Candel, A. M.; Beltrán, A.; Torrecillas, A.; He, L.; Jiang, Y.; Zhang, S.; Teruel, J. A.; Gómez-Fernández, J. C. A Comparison of the Location in Membranes of Curcumin and Curcumin-Derived Bivalent Compounds with Potential Neuroprotective Capacity for Alzheimer's Disease. *Colloids Surf., B* **2021**, *199*, 111525.
(33) Zou, X.; Himbert, S.; Dujardin, A.; Juhasz, J.; Ros, S.; Stöver, H. D. H.; Rheinstädter, M. C. Curcumin and Homotaurine Suppress Amyloid-B25−35Aggregation in Synthetic Brain Membranes. *ACS Chem. Neurosci.* **2021**, *12* (8), 1395−1405.
(34) Randino, R.; Grimaldi, M.; Persico, M.; De Santis, A.; Cini, E.; Cabri, W.; Riva, A.; D'Errico, G.; Fattorusso, C.; D'Ursi, A. M.; Rodriquez, M. Investigating the Neuroprotective Effects of Turmeric Extract: Structural Interactions of β-Amyloid Peptide with Single Curcuminoids. *Sci. Rep.* **2016**, *6*, 38846.
(35) Khondker, A.; Alsop, R. J.; Himbert, S.; Tang, J.; Shi, A. C.; Hitchcock, A. P.; Rheinstädter, M. C. Membrane-Modulating Drugs Can Affect the Size of Amyloid-β 25−35 Aggregates in Anionic Membranes. *Sci. Rep.* **2018**, *8* (1), 12367.
(36) Taylor, M.; Moore, S.; Mourtas, S.; Niarakis, A.; Re, F.; Zona, C.; Ferla, B. L.; Nicotra, F.; Masserini, M.; Antimisiaris, S. G.; Gregori, M.; Allsop, D. Effect of Curcumin-Associated and Lipid Ligand-Functionalized Nanoliposomes on Aggregation of the Alzheimer's Aβ Peptide. *Nanomedicine* **2011**, *7* (5), 541−550.
(37) Thapa, A.; Vernon, B. C.; De la Peña, K.; Soliz, G.; Moreno, H. A.; López, G. P.; Chi, E. Y. Membrane-Mediated Neuroprotection by Curcumin from Amyloid-β-Peptide- Induced Toxicity. *Langmuir* **2013**, *29* (37), 11713−11723.
(38) Seelig, A. Local Anesthetics and Pressure- a Comparison of Dibucaine Binding to Lipid Monolayers and Bilayers. *Biochim. Biophys. Acta* **1987**, *899* (2), 196−204.
(39) Yu, X.; Zheng, J. Cholesterol Promotes the Interaction of Alzheimer β-Amyloid Monomer with Lipid Bilayer. *J. Mol. Biol.* **2012**, *421* (4−5), 561−571.
(40) Yang, H.; Yang, S.; Kong, J.; Dong, A.; Yu, S. Obtaining Information about Protein Secondary Structures in Aqueous Solution Using Fourier Transform IR Spectroscopy. *Nat. Protoc.* **2015**, *10* (3), 382−396.
(41) Waeytens, J.; Van Hemelryck, V.; Deniset-Besseau, A.; Ruysschaert, J. M.; Dazzi, A.; Raussens, V. Characterization by Nano-Infrared Spectroscopy of Individual Aggregated Species of Amyloid Proteins. *Molecules* **2020**, *25* (12), 2899.
(42) Fändrich, M. Oligomeric Intermediates in Amyloid Formation: Structure Determination and Mechanisms of Toxicity. *J. Mol. Biol.* **2012**, *421* (4−5), 427−440.
(43) Zandomeneghi, G.; Krebs, M. R. H.; McCammon, M. G.; Fändrich, M. FTIR Reveals Structural Differences between Native β-Sheet Proteins and Amyloid Fibrils. *Protein Sci.* **2004**, *13* (12), 3314−3321.
(44) Lyu, Y.; Xiang, N.; Mondal, J.; Zhu, X.; Narsimhan, G. Characterization of Interactions between Curcumin and Different Types of Lipid Bilayers by Molecular Dynamics Simulation. *J. Phys. Chem. B* **2018**, *122* (8), 2341−2354.
(45) Mahieu, E.; Ibrahim, Z.; Moulin, M.; Härtlein, M.; Franzetti, B.; Martel, A.; Gabel, F. The Power of SANS, Combined with Deuteration and Contrast Variation, for Structural Studies of Functional and Dynamic Biomacromolecular Systems in Solution. *EPJ Web Conf.* **2020**, *236*, 03002.
(46) Serpell, L. C. Alzheimer's Amyloid Fibrils: Structure and Assembly. *Biochim. Biophys. Acta* **2000**, *1502*, 16−30.
(47) Sun, Y.; Lee, C. C.; Hung, W. C.; Chen, F. Y.; Lee, M. T.; Huang, H. W. The Bound States of Amphipathic Drugs in Lipid Bilayers: Study of Curcumin. *Biophys. J.* **2008**, *95* (5), 2318−2324.
(48) Leite, N. B.; Martins, D. B.; Fazani, V. E.; Vieira, M. R.; dos Santos Cabrera, M. P. Cholesterol Modulates Curcumin Partitioning and Membrane Effects. *Biochim. Biophys. Acta, Biomembr.* **2018**, *1860* (11), 2320−2328.
(49) Ingólfsson, H. I.; Thakur, P.; Herold, K. F.; Hobart, E. A.; Ramsey, N. B.; Periole, X.; De Jong, D. H.; Zwama, M.; Yilmaz, D.; Hall, K.; Maretzky, T.; Hemmings, H. C.; Blobel, C.; Marrink, S. J.; Koçer, A.; Sack, J. T.; Andersen, O. S. Phytochemicals Perturb Membranes and Promiscuously Alter Protein Function. *ACS Chem. Biol.* **2014**, *9* (8), 1788−1798.
(50) Hung, W. C.; Chen, F. Y.; Lee, C. C.; Sun, Y.; Lee, M. T.; Huang, H. W. Membrane-Thinning Effect of Curcumin. *Biophys. J.* **2008**, *94* (11), 4331−4338.
(51) Ingolfsson, H. I.; Koeppe, R. E.; Andersen, O. S. Curcumin Is a Modulator of Bilayer Material Properties. *Biochemistry* **2007**, *46* (36), 10384−10391.
(52) Lee, W.; Lee, D. G. An antifungal mechanism of curcumin lies in membrane-targeted action within *Candida albicans*. *IUBMB Life* **2014**, *66* (11), 780−785.
(53) Bode, D. C.; Freeley, M.; Nield, J.; Palma, M.; Viles, J. H. Amyloid-β Oligomers Have a Profound Detergent-like Effect on Lipid Membrane Bilayers, Imaged by Atomic Force and Electron Microscopy. *J. Biol. Chem.* **2019**, *294* (19), 7566−7572.
(54) Ngoc, L. L. N.; Itoh, S. G.; Sompornpisut, P.; Okumura, H. Replica-Permutation Molecular Dynamics Simulations of an Amyloid-β(16−22) Peptide and Polyphenols. *Chem. Phys. Lett.* **2020**, *758*, 137913.
(55) Ono, K.; Li, L.; Takamura, Y.; Yoshiike, Y.; Zhu, L.; Han, F.; Mao, X.; Ikeda, T.; Takasaki, J.; Nishijo, H.; Takashima, A.; Teplow, D. B.; Zagorski, M. G.; Yamada, M. Phenolic Compounds Prevent Amyloid-Protein Oligomerization and Synaptic Dysfunction by Site-Specific Binding. *J. Biol. Chem.* **2012**, *287* (18), 14631−14643.
(56) Matsubara, T.; Yasumori, H.; Ito, K.; Shimoaka, T.; Hasegawa, T.; Sato, T. Amyloid- Fibrils Assembled on Ganglioside-Enriched Membranes Contain Both Parallel -Sheets and Turns. *J. Biol. Chem.* **2018**, *293* (36), 14146−14154.
(57) Hoshino, T.; Mahmood, M. I.; Mori, K.; Matsuzaki, K. Binding and Aggregation Mechanism of Amyloid β-Peptides onto the GM1 Ganglioside-Containing Lipid Membrane. *J. Phys. Chem. B* **2013**, *117* (27), 8085−8094.
(58) Kang, S. G.; Han, Z. Z.; Daude, N.; McNamara, E.; Wohlgemuth, S.; Molina-Porcel, L.; Safar, J. G.; Mok, S. A.; Westaway, D. Pathologic Tau Conformer Ensembles Induce Dynamic, Liquid-Liquid Phase Separation Events at the Nuclear Envelope. *BMC Biol.* **2021**, *19* (1), 199.
(59) Galvagnion, C.; Buell, A. K.; Meisl, G.; Michaels, T. C. T.; Vendruscolo, M.; Knowles, T. P. J.; dobson, C. M. Lipid vesicles trigger α-synuclein aggregation by stimulating primary nucleation. *Nat. Chem. Biol.* **2015**, *11*, 229−234.
(60) Breydo, L.; Kurouski, D.; Rasool, S.; Milton, S.; Wu, J. W.; Uversky, V. N.; Lednev, I. K.; Glabe, C. G. Structural Differences

https://doi.org/10.1021/acschemneuro.3c00512
ACS Chem. Neurosci. 2023, 14, 4026−4038

between Amyloid Beta Oligomers. *Biochem. Biophys. Res. Commun.* **2016**, *477* (4), 700−705.
(61) Als-Nielsen, J.; Kjær, K. X-Ray Reflectivity and Diffraction Studies of Liquid Surfaces and Surfactant Monolayers. *Phase Transitions in Soft Condensed Matter*; Springer, 1989; pp 113−138.
(62) Als-Nielsen, J.; Jacquemain, D.; Kjaer, K.; Leveiller, F.; Lahav, M.; Leiserowitz, L. Principles and Applications of Grazing Incidence X-Ray and Neutron Scattering from Ordered Molecular Monolayers at the Air-Water Interface. *Phys. Rep.* **1994**, *246*, 251−313.
(63) Jensen, T. R.; Kjaer, K. Structural Properties and Interactions of Thin Films at the Air-Liquid Interface Explored by Synchrotron x-Ray Scattering. *Novel Methods to Study Interfacial Layers*; Elsevier, 2001; Vol. *11*, pp 205−254.
(64) Kjaer, K. Some Simple Ideas on X-Ray Reflection and Grazing-Incidence Diffraction from Thin Surfactant Films. *Phys. B* **1994**, *198*, 100−109.
(65) Nelson, A. Co-Refinement of Multiple-Contrast Neutron/X-Ray Reflectivity Data Using MOTOFIT. *J. Appl. Crystallogr.* **2006**, *39*, 273−276.
(66) Pedersen, J. S.; Hamley, I. W. Analysis of Neutron and X-Ray Reflectivity Data by Constrained Least-Squares Methods. *Phys. B* **1994**, *198* (1−3), 16−23.
(67) Watkins, E. B.; Miller, C. E.; Mulder, D. J.; Kuhl, T. L.; Majewski, J. Structure and Orientational Texture of Self-Organizing Lipid Bilayers. *Phys. Rev. Lett.* **2009**, *102* (23), 238101.
(68) Guinier, A. *X-Ray Diffraction in Crystals, Imperfect Crystals, and Amorphous Bodies*; W.H. Freeman: San Francisco, 1963.
(69) Lee, J.; Cheng, X.; Swails, J. M.; Yeom, M. S.; Eastman, P. K.; Lemkul, J. A.; Wei, S.; Buckner, J.; Jeong, J. C.; Qi, Y.; Jo, S.; Pande, V. S.; Case, D. A.; Brooks, C. L.; MacKerell, A. D.; Klauda, J. B.; Im, W. CHARMM-GUI Input Generator for NAMD, GROMACS, AMBER, OpenMM, and CHARMM/OpenMM Simulations Using the CHARMM36 Additive Force Field. *J. Chem. Theory Comput.* **2016**, *12* (1), 405−413.
(70) Lyu, Y.; Xiang, N.; Mondal, J.; Zhu, X.; Narsimhan, G. Characterization of Interactions between Curcumin and Different Types of Lipid Bilayers by Molecular Dynamics Simulation. *J. Phys. Chem. B* **2018**, *122* (8), 2341−2354.
(71) Kandt, C.; Ash, W. L.; Peter Tieleman, D. Setting up and Running Molecular Dynamics Simulations of Membrane Proteins. *Methods* **2007**, *41*, 475−488.
(72) Paravastu, A. K.; Leapman, R. D.; Yau, W. M.; Tycko, R. Molecular Structural Basis for Polymorphism in Alzheimer's β-Amyloid Fibrils. *Proc. Natl. Acad. Sci. U.S.A.* **2008**, *105* (47), 18349−18354.
(73) Huang, J.; Rauscher, S.; Nawrocki, G.; Ran, T.; Feig, M.; De Groot, B. L.; Grubmüller, H.; Mackerell, A. D. CHARMM36m: An Improved Force Field for Folded and Intrinsically Disordered Proteins. *Nat. Methods* **2017**, *14* (1), 71−73.
(74) Abraham, M. J.; Murtola, T.; Schulz, R.; Páll, S.; Smith, J. C.; Hess, B.; Lindahl, E. Gromacs: High Performance Molecular Simulations through Multi-Level Parallelism from Laptops to Supercomputers. *SoftwareX* **2015**, *1−2*, 19−25.
(75) Vanommeslaeghe, K.; Hatcher, E.; Acharya, C.; Kundu, S.; Zhong, S.; Shim, J.; Darian, E.; Guvench, O.; Lopes, P.; Vorobyov, I.; Mackerell, A. D. CHARMM General Force Field: A Force Field for Drug-Like Molecules Compatible with the CHARMM All-Atom Additive Biological Force Fields. *J. Comput. Chem.* **2010**, *31*, 671−690.
(76) Humphrey, W.; Dalke, A.; Schulten, K. VMD: Visual Molecular Dynamics. *J. Mol. Graphics* **2006**, *14* (1), 33−38.

https://doi.org/10.1021/acschemneuro.3c00512
ACS Chem. Neurosci. 2023, 14, 4026−4038